Islands of instability for growth of spiral vortices in the Taylor-Couette system with and without axial through flow

S. Altmeyer, Ch. Hoffmann, and M. Lücke
Institut für Theoretische Physik, Universität des Saarlandes, Postfach 151150, D-66123 Saarbrücken, Germany
(Received 28 February 2011; published 11 October 2011)

We present numerical calculations of the linearized Navier-Stokes equations for axially extended and axially localized spiral structures in the Taylor-Couette system. The eigenvalue surface for spiral vortices with azimuthal wave number $M = 2$ shows significantly more structure than that for vortices with $M = 0$ and 1. Islands are found in parameter space where axially periodic vortex perturbations can grow. Bicriticality of different axial wave numbers is observed. Furthermore, parameter islands of absolute instability are found where wave packets consisting of near-critical extended perturbations can grow and expand via oppositely moving fronts. Some results are compared with those of the Ginzburg-Landau approximation.

DOI: 10.1103/PhysRevE.84.046308 PACS number(s): 47.20.Ky, 47.32.−y, 47.54.−r

I. INTRODUCTION

The Taylor-Couette system [1–3] consisting of a viscous, isothermal fluid confined in the annulus between two concentric, independently rotating cylinders is a prototypical example for bifurcation theory in hydrodynamics. It is one of the simplest driven nonlinear dissipative systems that shows spontaneous pattern formation out of an unstructured basic state [1,3–5]. For the axial periodic boundary conditions that we consider here, the stationary, axially, and azimuthally homogeneous basic flow consists of a superposition of the circular Couette flow (CCF) driven by the rotating cylinders and of the annular Poiseuille flow (APF) generated by an externally imposed axial through flow [4,6].

For sufficiently strong rotation speeds, spiral vortices with azimuthal wave numbers $M \neq 0$ occur in the basic state via a symmetry-breaking Hopf bifurcation as a result of a linear instability [5,7–9]. These spirals are traveling waves in the axial direction and rotating waves in the azimuthal direction. The primary bifurcation to such periodic vortex structures has been the aim of many linear stability analyses of the basic state [9–14]. Moreover, an investigation of convective and absolute instability is presented in [15].

In this paper, we investigate extended as well as localized linear perturbations with azimuthal wave number $M = 2$ in a wide range of through flow and inner and outer cylinder velocities. This is done by numerically solving the eigenvalue problem of the linearized Navier-Stokes equations (NSE) for real and for complex axial wave numbers. We use a shooting method with a fourth-order Runge-Kutta algorithm to determine the radial dependence of the eigenfunctions. Furthermore, the boundaries of absolute and convective instability and the characteristic properties of linear vortex fronts are determined by a saddle-point analysis of the complex dispersion relation of the NSE evaluated for complex axial wave numbers [16–18]. These results are compared also with predictions of the classical Ginzburg-Landau equations (GLE) [4,19].

For $M = 2$ spiral vortices (2 SPI), we find for certain parameters a peculiar behavior that has not been seen for either $M = 0$ Taylor vortex perturbations or $M = 1$ spirals that have been studied extensively [5,8–14,20]: (i) "islands" in parameter space for the growth of axially periodic 2 SPI structures that are surrounded by a stability regime of the basic state. Such islands have already been observed in other settings [21]; (ii) "islands" of absolute instability for the growth of near-critical localized wave packets of 2 SPI perturbations that are enclosed by convective instability.

These effects are a consequence of a rather complex eigenvalue surface of the 2 SPI solutions of the linear NSE and of the somewhat unusual behavior of the relevant saddle nodes of the dispersion relation, neither of which is captured by the GLE.

The first part of the paper concerns the marginal and critical bifurcation thresholds for extended vortex structures with different azimuthal wave numbers $M \leqslant 2$. In the second part, we investigate localized wave packets that consist in particular of near-critical extended 2 SPI perturbations. We focus on the spatiotemporal behavior of their fronts using a saddle-point analysis and we determine the boundary between convective and absolute instability of the basic flow against these 2 SPI perturbations.

II. SYSTEM

We present numerical results for vortex perturbations in axially unbounded Taylor-Couette systems with counter-rotating cylinders and externally imposed axial flow. The gap width between the outer cylinder of radius r_2 and the inner one of radius r_1 is $d = r_2 - r_1$. With infinitely long cylinders, the only relevant parameter characterizing the geometry is the radius ratio $\eta = r_1/r_2$. The latter is fixed here to be $\eta = 0.5$.

The fluid in the annulus is taken to be isothermal and incompressible with kinematic viscosity ν. To characterize the driving of the system, we use the Reynolds numbers

$$R_1 = r_1\Omega_1 d/\nu, \quad R_2 = r_2\Omega_2 d/\nu. \tag{2.1}$$

They are the reduced azimuthal velocities of the fluid at the inner and outer cylinder, respectively, where Ω_1 and Ω_2 are the respective angular velocities of the cylinders. The inner one is always rotating counterclockwise so that Ω_1 and R_1 are positive.

 ©2011 American Physical Society

An externally imposed axial through flow is measured by the axial Reynolds number

$$\mathrm{Re} = \frac{d}{\nu}\langle w\rangle, \tag{2.2}$$

where the mean axial velocity $\langle w\rangle$ averaged over the annular cross section describes the total through flow.

We use also the relative control parameters

$$\mu = \frac{R_1}{R_{1,c}(\mathrm{Re})} - 1, \quad \epsilon = \frac{R_1}{R_{1,c}(\mathrm{Re}=0)} - 1, \tag{2.3}$$

measuring the relative distance of the inner Reynolds number R_1 from the critical onset $R_{1,c}$ of the axially extended spiral vortex or Taylor vortex patterns in the presence and in the absence ($\mathrm{Re} = 0$) of through flow, respectively. In this notation,

$$\mu_c = 0 \quad \text{and} \quad \epsilon_c(\mathrm{Re}) = \frac{R_{1,c}(\mathrm{Re})}{R_{1,c}(\mathrm{Re}=0)} - 1 \tag{2.4}$$

is the critical threshold for the onset of the vortex flow in question. The relation between μ and ϵ is

$$\mu = \frac{\epsilon - \epsilon_c(\mathrm{Re})}{1+\epsilon_c(\mathrm{Re})}. \tag{2.5}$$

In the following, we scale positions by the gap width d, the velocity $\mathbf{u}$ by the velocity $r_1\Omega_1$ of the inner cylinder, time t by the momentum diffusion time d^2/ν across the gap, and the pressure p by $\rho r_1\Omega_1\nu/d$, with ρ denoting the constant mass density of the fluid. Furthermore, we decompose the velocity field

$$\mathbf{u} = u\mathbf{e}_r + v\mathbf{e}_\varphi + w\mathbf{e}_z \tag{2.6}$$

into radial (u), azimuthal (v), and axial (w) components using cylindrical coordinates r, φ, and z.

The basic flow state $\mathbf{u}_g$ that is realized for Reynolds numbers R_1 below the thresholds for the onset of Taylor and spiral vortex flow is rotationally symmetric, axially homogeneous, and constant in time. It consists of a linear superposition of circular Couette flow in the azimuthal direction, $\mathbf{e}_\varphi$, and of annular Poiseuille flow in the axial direction, $\mathbf{e}_z$,

$$\mathbf{u}_g = v_{\mathrm{CCF}}(r)\mathbf{e}_\varphi + w_{\mathrm{APF}}(r)\mathbf{e}_z \tag{2.7}$$

without any radial component. Here

$$v_{\mathrm{CCF}}(r) = Ar + B/r \tag{2.8}$$

and

$$w_{\mathrm{APF}}(r) = \mathrm{Re}\frac{r^2 + C\ln(r) + D}{E}, \tag{2.9}$$

with constants A–E given in Ref. [20].

The Navier-Stokes equations for the deviation fields $\mathbf{u}$ and p from the above-described basic state read after linearization in the deviations

$$\partial_t\mathbf{u} = \nabla^2\mathbf{u} - R_1(\mathbf{u}_g\cdot\nabla)\mathbf{u} - R_1(\mathbf{u}\cdot\nabla)\mathbf{u}_g - \nabla p. \tag{2.10}$$

We expand the solution of Eq. (2.10) into azimuthal and axial Fourier modes

$$\mathbf{u}(r,\varphi,z,t) = \sum_{m,n}\hat{\mathbf{u}}_{m,n}(r,t)e^{i(m\varphi+nkz)}. \tag{2.11}$$

Here k is the axial wave number, which is taken to be positive. The time dependence of the complex mode amplitudes is exponential,

$$\hat{\mathbf{u}}_{m,n}(r,t) = \hat{\mathbf{u}}_{m,n}(r)e^{\sigma t}, \tag{2.12}$$

with complex characteristic exponents

$$\sigma = \mathrm{Re}(\sigma) + i\,\mathrm{Im}(\sigma) = \gamma - i\omega \tag{2.13}$$

that depend in general on the mode indices, the wave number, and the three Reynolds numbers. Here γ is the growth rate and ω is the characteristic frequency of the mode in question.

III. AXIALLY EXTENDED VORTEX STRUCTURES

In this section, we consider perturbations of the basic state in the form of axially extended, periodic vortex structures with axial wave number k and azimuthal wave number $M = 0,1,2$. The critical modes are $n = \pm1, m = M = 0$ for rotationally symmetric Taylor vortex flow (TVF) and $n = \pm1, m = nM$ for left-handed spiral vortex flow (LM SPI) with azimuthal wave number M, and $n = \pm1, m = -nM$ for right-handed spiral vortex flow (RM SPI) with azimuthal wave number M. In Fig. 1, we show the structure of TVF, L1 SPI, and L2 SPI schematically with the help of isosurfaces of the azimuthal vorticity.

Because of the $z \to -z$ symmetry of the Taylor-Couette system, we often discuss here only L SPI. Without through flow, L SPI and R SPI are mirror images of each other. Furthermore, in the presence of an axial through flow with Reynolds number Re, the physical properties of R SPI solutions of the NSE (2.10) are tied to those of L SPI solutions with the invariance of the NSE under axial reflection, $(z,w,\mathrm{Re}) \to (-z,-w,-\mathrm{Re})$; cf. [20] for more details. Thus, an R SPI at a Reynolds number Re behaves like the mirror image of an L SPI at $-\mathrm{Re}$.

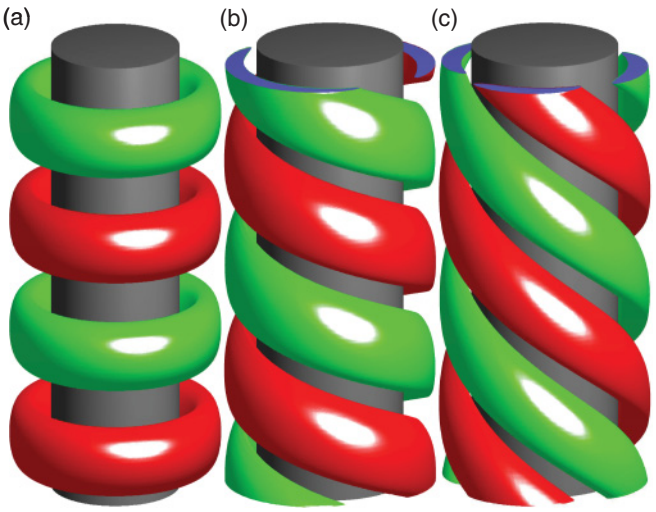

FIG. 1. (Color online) Isosurfaces of the azimuthal vorticity field $\partial_z u - \partial_r w$ for TVF (a), L1 SPI (b), and L2 SPI (c) close to their respective onsets. Here, $\mathrm{Re} = 0$ so that the R SPI are the axial mirror images of the corresponding L SPI structures. For finite through flow, an R SPI at Reynolds number Re is the mirror image of the corresponding L SPI at $-\mathrm{Re}$.

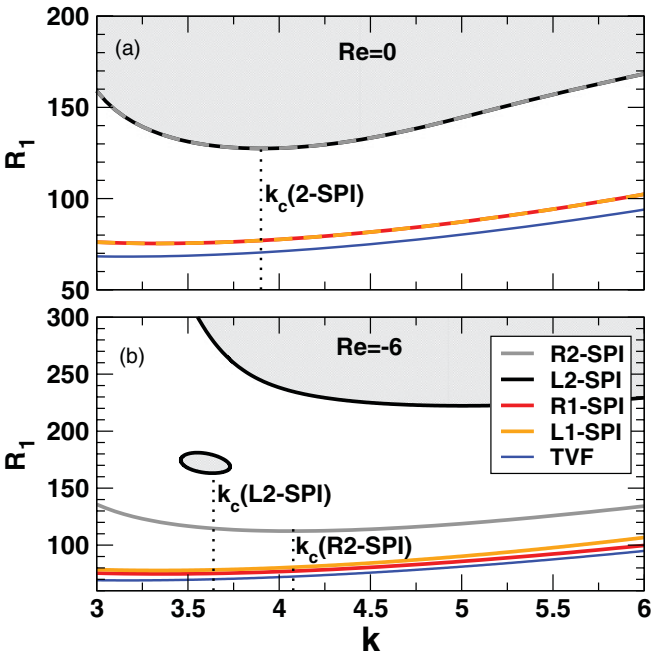

FIG. 2. (Color online) Marginal stability curves of the basic state against vortex perturbations at $R_2 = 0$ with azimuthal wave numbers $M = 0, 1, 2$ for Re $= 0$ (a) and Re $= -6$ (b). For the latter, there is an isolated island of instability against L2 SPI. Vertical dotted lines indicate the critical wave numbers for 2 SPI as indicated.

A. Axial through flow

We first consider in Fig. 2 the marginal stability curves of the basic state against vortex perturbations with azimuthal wave numbers $M = 0$, 1, and 2 and fixed outer cylinder, $R_2 = 0$. These stability curves are the bifurcation thresholds for TVF, 1 SPI, and 2 SPI, respectively. Since these extended vortex structures typically bifurcate forward, the marginal stability curves give reliable information for what parameters one can expect to find such structures in experiments. Finite axial through flow lifts the symmetry degeneracy of L SPI and R SPI as described in detail in [6,20]. Furthermore, and in addition, the L2 SPI curve consists at Re $= -6$ of two separate parts defining disjunct (gray-shaded) regions with positive growth rates for L2 SPI modes.

In order to elucidate the origin of the two disconnected marginal stability curves related to L2 SPI perturbations, we present in Fig. 3 the surfaces of the linear growth rates γ of TVF, L1 SPI, and L2 SPI modes over the k-R_1 plane for $R_2 = 0$,Re $= -6$. The marginal stability thresholds are the $\gamma = 0$ isolines of these "mountain landscapes." In contrast to the monotonically varying surfaces for TVF and L1 SPI modes in (a) and (b), the mountain landscape for the L2 SPI mode in Fig. 3(c) has a saddle and a small "hill." Parts of the hill lie above the $\gamma = 0$ isoline, which is shown there by a thick (red) curve for better visibility.

The shape of this mountain landscape for the L2 SPI mode is almost independent of Re and R_2; cf. below. Varying Re simply shifts the whole mountain toward lower or higher γ. In this way, the island in Fig. 2(b) disappears for sufficiently large negative Re when the top of the hill gets lowered below $\gamma = 0$. On the other hand, the island gets connected with the

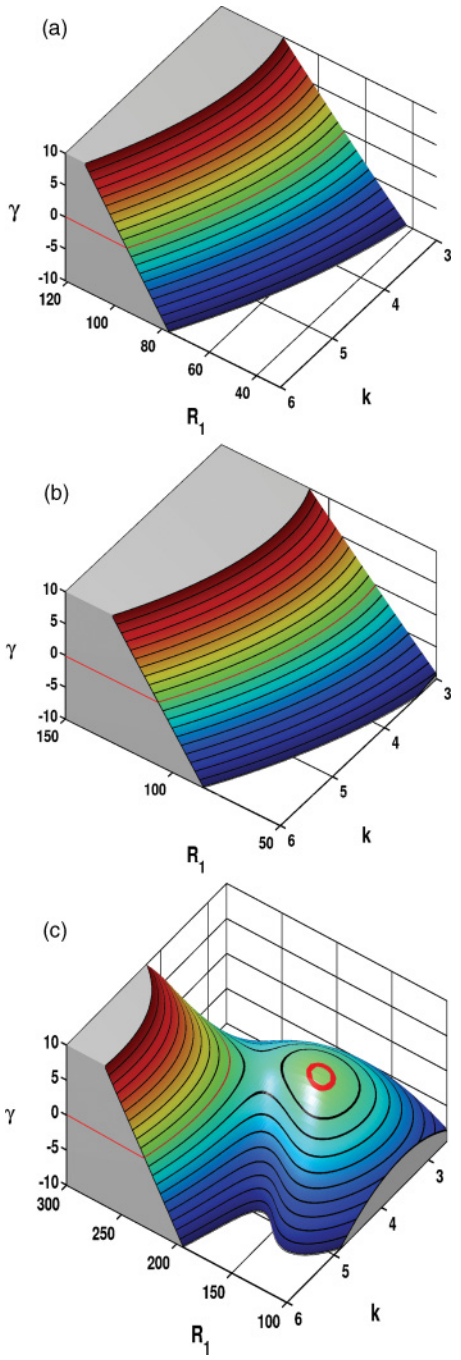

FIG. 3. (Color online) Surfaces of the linear growth rate γ over the k-R_1 plane for TVF (a), L1 SPI (b), and L2 SPI (c). In each case, $R_2 = 0$ and Re $= -6$ as in Fig. 2(b). The red (gray) $\gamma = 0$ isolines identify the marginal curves. The characteristic shape of the γ surface for L2 SPI modes causes the corresponding marginal curve to split into two separated parts; cf. Fig. 2(b).

main gray instability region of Fig. 2(b) when for sufficiently small negative Re the saddle in Fig. 3(c) is lifted above $\gamma = 0$.

This is illustrated in Fig. 4. There we show marginal stability surfaces, $\gamma = 0$, for L2 SPI modes in k-R_1-Re parameter space at $R_2 = 0$ (a1) and in k-R_1-R_2 space at Re $= -6$ (b1). In (a2), we show for $R_2 = 0$ several marginal curves in the k-R_1 plane for different Re. Similarly, in (b2) marginal curves for Re $= -6$ are shown for different R_2. The

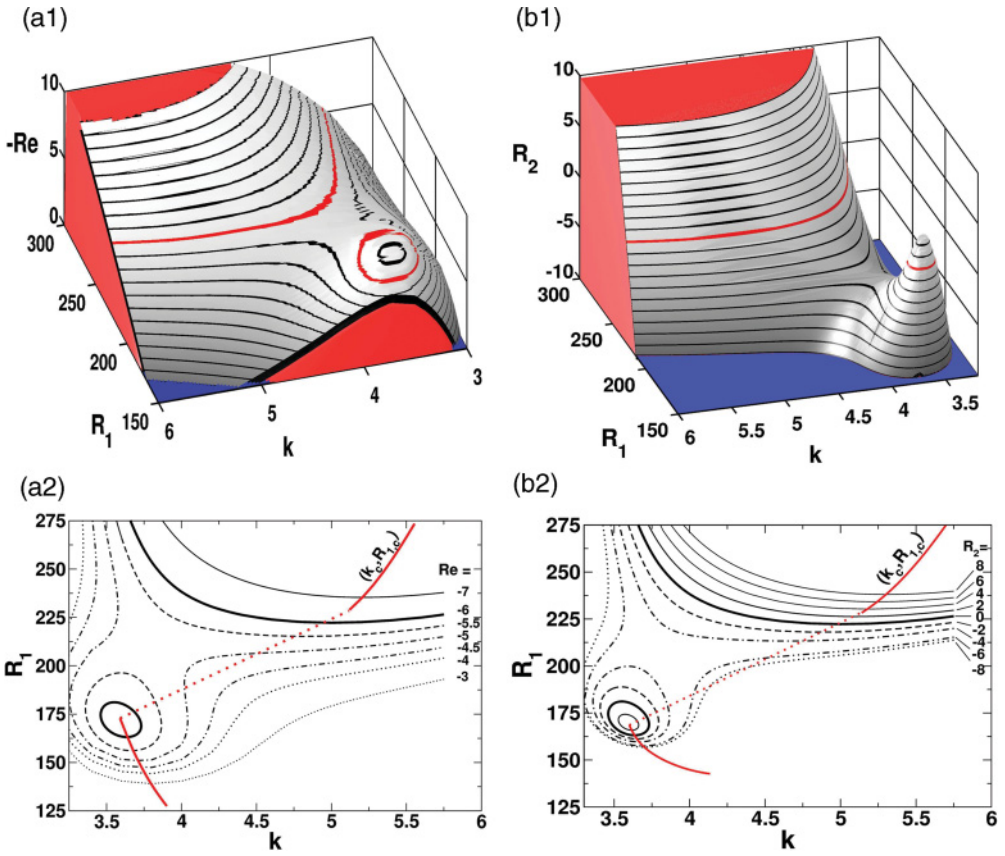

FIG. 4. (Color online) Marginal stability surfaces, $\gamma = 0$, for L2 SPI modes in k-R_1-Re parameter space at $R_2 = 0$ (a1) and in k-R_1-R_2 space at $\mathrm{Re} = -6$ (b1). The surfaces separate the parameter spaces into regions with $\gamma < 0$ (above the surfaces) and regions with $\gamma > 0$ (below the surfaces). Marginal curves in the k-R_1 plane are shown in (a2) for different Re at $R_2 = 0$ and in (b2) for different R_2 at $\mathrm{Re} = -6$. The thick red (gray) $\gamma = 0$ isolines in (a1) at $\mathrm{Re} = -6$ and in (b1) at $R_2 = 0$ correspond to the respective thick black lines in (a2) and (b2), respectively. The variation of the critical points $(k_c, R_{1,c})$ with Re and R_2 is shown in (a2) and (b2), respectively, by full red (gray) lines that are labeled accordingly. The jump of the critical point is indicated by dotted red (gray) lines.

thick red (gray) $\gamma = 0$ isolines in (a1) at $\mathrm{Re} = -6$ and in (b1) at $R_2 = 0$ correspond to the respective thick black lines in (a2) and (b2). The variation of the critical points $(k_c, R_{1,c})$ with Re and R_2 is shown in (a2) and (b2), respectively, by full red (gray) lines that are labeled accordingly. The jump of the critical point is indicated by dotted red (gray) lines.

Consider first how the structure of L2 SPI marginality in parameter space changes at fixed $R_2 = 0$ when Re varies. Decreasing Re from zero to negative values, i.e., moving vertically upward in Fig. 4(a1), the saddle occurs at $\mathrm{Re} \approx -5.1$. At this isoline, the part of the mountain in Fig. 4(a1) that is protruding to the lower right is disconnected from the main part. So, the downward bulging marginal curves in Fig. 4(a2) pinch off at $\mathrm{Re} \approx -5.1$ and form an island in the lower left of Fig. 4(a2). Decreasing Re to more negative values, i.e., moving vertically further upward in Fig. 4(a1), one reaches the top of the hill at $\mathrm{Re} \approx -6.4$, and the island in Fig. 4(a2) shrinks to a point and then disappears.

If one fixes the through flow, say, at $\mathrm{Re} = -6$ and varies the outer Reynolds number instead, as done in Fig. 4(b), then one observes practically the same structural changes in the L2 SPI marginality locations in parameter space as for the variations of Re in Fig. 4(a). Thus, changing the through flow and changing the rotation rate of the outer cylinder have similar effects on the bifurcation thresholds of L2 SPI.

This similarity in behavior when Re or R_2 is changed holds also for the critical values $k_c, R_{1,c}$, and ω_c of L2 SPI that are shown in Fig. 5. Note their discontinuities (dotted vertical lines in Fig. 5) when the island structure disappears: in Figs. 5(a) and 4(a) at $\mathrm{Re} \approx -6.4$ and in Figs. 5(b) and 4(b) at $R_2 = 2.3$. The striped bars in Fig. 5 mark the parameter intervals ($-6.4 < \mathrm{Re} < -5.1$ and $-5.2 < R_2 < 2.3$, respectively) in which the marginal curves display an instability island that is surrounded by stability and that is separated from the main instability region in the k-R_1 plane in Fig. 4.

Without through flow ($\mathrm{Re} = 0$), L and R SPI are symmetry-degenerated so that their critical values k_c and $R_{1,c}$ are the same and their frequencies differ only by a sign. The external axial through flow lifts the degeneracy [20,22], e.g., the onsets of upstream (downstream) propagating SPI are shifted toward larger (smaller) R_1. Thus, in the Re range shown in Fig. 5, the bifurcation thresholds for L1 and L2 SPI lie above those of R1 and R2 SPI, respectively.

The critical axial wave numbers for L2 SPI (Fig. 5) behave significantly different from those of R2 SPI or L1 and R1 SPI. This also holds for the critical Reynolds numbers $R_{1,c}$ and the critical frequencies ω_c (c). All but the L2 wave numbers

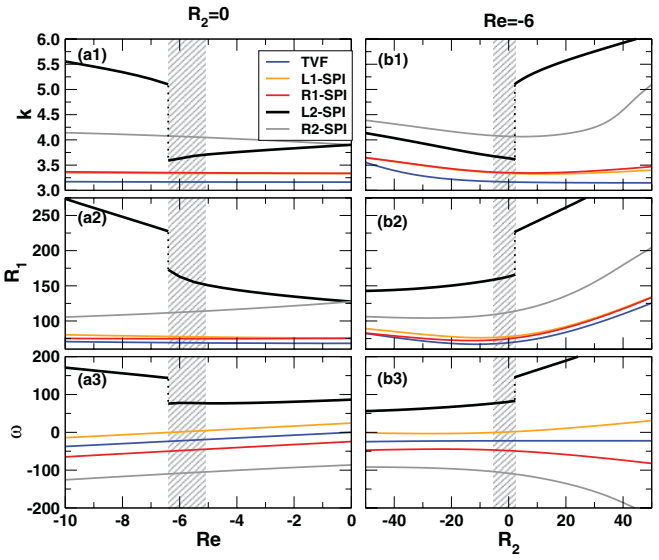

FIG. 5. (Color online) Critical axial wave numbers k_c, critical Reynolds numbers $R_{1,c}$, and critical frequencies ω_c for TVF, 1 SPI, and 2 SPI vs axial through flow Re (a) and R_2 (b). The striped bars mark the intervals in which the L2 SPI marginal curve is split into two separated parts so that an isolated instability island for L2 SPI modes exists. When the island disappears, the critical values undergo a jump indicated by the dotted vertical lines.

increase with increasing |Re|. So, e.g., for $R_2 = 0$ and negative Re, the upstream (in the positive z direction) propagating L2 SPI selects a wave number that first increases with the axial "head wind." Then, at Re ≈ -6.4, it jumps to a significantly larger wave number so that thereafter the critical wave number for the L2 SPI mode is larger than that for the R2 SPI. This is a significant difference from the $M = 1$ case, in which k_c(R1 SPI) always lies above k_c(L1 SPI), independently of Re or R_2.

B. Counter-rotating cylinders

Roughly speaking, the γ surface of Fig. 3(c) moves as a whole also when R_2 is varied at fixed Re in a way that is quite similar to the above discussed situation in which one varies Re at fixed R_2. In particular, one can find an interval of R_2 values where the saddle in Fig. 3(c) lies below the $\gamma = 0$ level while part of the hill lies above it so that the $\gamma = 0$ isoline consists of two separate curves in the k-R_1 plane. For Re $= -6$, this situation with an instability island in the k-R_1 plane that is enclosed by the marginal curve occurs for $-5.2 < R_2 < 2.3$. So, one simply has to vary either Re or R_2 in order to move the $\gamma = 0$ level into the area between the saddle and the top of the hill.

However, we want to stress that the evolution scenarios of the γ landscapes for L2 SPI perturbations as described above with the island formation by the marginal L2 curves occur only when the through flow is sufficiently strong, namely, only when Re $\lesssim -0.1$. We found that for Re > -0.1 there exists no R_2 with isolated islands for L2 SPI growth in the k-R_1 plane.

In Fig. 5(b), we have chosen as a representative example Re $= -6$, which lies within the above-mentioned Re interval. We show the critical axial wave number k_c, Reynolds number $R_{1,c}$, and frequency ω_c versus R_2 for TVF, 1 SPI, and 2 SPI. The striped regions mark the interval in which the L2 SPI marginal curve is split into two separate parts and in which an isolated instability "island" for L2 SPI modes exists in the k-R_1 plane.

While the critical quantities of TVF, L1 SPI, R1 SPI, and R2 SPI show as functions of R_2 the smooth "classical" behavior in Fig. 5(b), the critical curves for the L2 SPI mode show jumps at $R_2 \approx 2.3$ in analogy to the situation in Fig. 5(a) that is discussed in the preceding section. In both cases, the jumps occur when the islands enclosed by the marginal stability curves in the k-R_1 plane disappear. The striped R_2 interval in Fig. 5(b) represents the R_2 values between the saddle and the local maximum at the top of the hill in the plot of Fig. 4(b1) showing the $\gamma = 0$ isosurface in k-R_1-R_2 space.

Last in this section, we investigate the characteristic critical velocities. Figure 6(a) displays the critical axial phase velocity $w_{\rm ph} = \omega_c/k_c$ of extended vortex structures resulting from the critical quantities shown in Fig. 5(a). With decreasing through flow, i.e., with Re becoming more negative, the critical phase velocities of TVF, L1 SPI, R1 SPI, and R2 SPI decrease smoothly while that of L2 SPI first decreases but then increases. This is somewhat peculiar since for the axially upward propagating L SPI in the downward directed through flow, the strength of the "headwind" increases when Re becomes more negative. Nevertheless, the phase velocity of L2 SPI remains upward directed with increasing magnitude. Furthermore, $w_{\rm ph}$ of L2 SPI shows an upwards jump when the isolated instability island in the k-R_1 plane disappears at Re ≈ -6.4.

Figure 6(b) shows the corresponding critical group velocities $w_g = \frac{\partial\omega}{\partial k}|_c$. They all decrease smoothly when the downward directed through flow becomes stronger. Note, however, that the group velocity of L2 SPI perturbations undergoes at Re ≈ -6.4 a jump to a positive value when the critical wave number in Fig. 5(a1) jumps to a significantly larger one. This implies that for Re < -6.4, the center of a

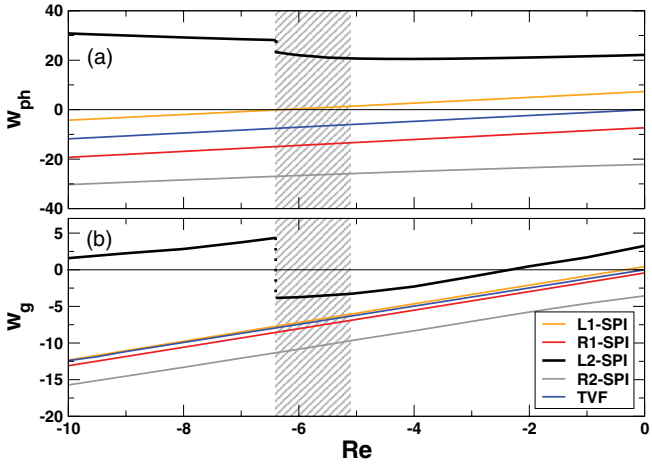

FIG. 6. (Color online) Critical axial phase velocity $w_{\rm ph} = \omega_c/k_c$ (a) and group velocity $w_g = \frac{\partial\omega}{\partial k}|_c$ (b) of TVF and SPI vs Re for $R_2 = 0$. The striped bars mark the interval in which the L2 SPI marginal curve is split into two separated parts so that an isolated instability island for L2 SPI modes exists. When the island disappears, the critical values undergo a jump indicated by the dotted vertical lines; see also Fig. 5(a).

wave packet consisting of the new near-critical L2 SPI modes with the larger wave numbers travels upstream, i.e., opposite to the through flow.

IV. LOCALIZED STRUCTURES

We now consider the spatiotemporal behavior of axially localized vortex structures consisting of linear wave packets of extended L SPI modes and of linear L SPI fronts. As in Sec. III, we discuss here explicitly the L SPI structures. The corresponding R SPI structures are related to them via the symmetry operation $(z,w,\mathrm{Re}) \to (-z,-w,-\mathrm{Re})$ [20]. Here the nonlinear behavior of initially infinitesimal localized perturbations might be quite different from the linear one. For example, nonlinear SPI fronts could display different dynamics from the linear ones. In addition, Ekman vortex modes that are present in finite systems can be expected to influence the localized SPI structures.

The analysis is based upon the knowledge of the complex temporal eigenvalue $\sigma(Q) = \gamma(Q) - i\omega(Q)$ of the vortex mode

$$\mathbf{u} \propto e^{i(Qz+m\varphi)+\sigma t} \tag{4.1}$$

with the azimuthal wave number m in question. This eigenvalue of the NSE (2.10) has to be evaluated with the above mode ansatz as a function of the complex axial wave number $Q = k - iK$. Here, as before, k is the real axial wave number and K denotes the axial spatial growth rate of $\mathbf{u}$ (4.1). Inserting the ansatz (4.1) into the NSE (2.10) allows us to evaluate the eigenvalue $\sigma(Q)$, e.g., with a shooting method as described in Ref. [20].

For comparison with the dispersion relation $\sigma(Q)$ of the NSE, we also analyzed the approximate dispersion relation $\sigma_{\mathrm{GLE}}(Q)$ of linear vortex modes following from the linear Ginzburg-Landau amplitude equation (GLE) [4],

$$\tau_0(\partial_t + w_g\partial_z)A = \left[(1+ic_0)\mu + (1+ic_1)\xi_0^2\partial_z^2\right]A \tag{4.2}$$

for the axially and temporally slowly varying complex amplitude $A(z,t)$ of a critical vortex mode $\propto e^{i(k_c z+m\varphi-\omega_c t)}$. One obtains [20]

$$\sigma_{\mathrm{GLE}}(Q) = -i\omega_c - i(Q-k_c)w_g + (1+ic_0)\frac{\mu}{\tau_0} - (1+ic_1)\frac{{\xi_0}^2}{\tau_0}(Q-k_c)^2. \tag{4.3}$$

The linear Ginzburg-Landau coefficients w_g, τ_0, ξ_0, c_0, and c_1 that enter into the above dispersion relation (4.3) are evaluated at criticality, $\gamma_c = 0, Q = k_c$ [20]. Like k_c and ω_c, they depend also on m, R_2, and Re. This dependence is not indicated explicitly here.

A. Convective and absolute instability

Concerning the linear growth and decay behavior of vortex perturbations of the basic flow state, one has to distinguish between three regimes: In the absolutely stable regime, any perturbation is damped. In the convectively unstable regime, some axially periodic, i.e., extended perturbations with wave numbers out of a band with finite width can grow together with their wave-packet superpositions. However, both fronts of the packet move in the same direction so that it is blown out of the system while its amplitude grows. In the absolutely unstable parameter region, the packet grows and expands when its two fronts move in opposite directions.

Thus, the transition from the convectively unstable to the absolutely unstable regime of the basic flow state against growth of spatially localized perturbations with a particular azimuthal wave number and with near-critical axial wave numbers k is accompanied by the reversal of the propagation direction of one of both fronts of a wave-packet perturbation in the laboratory frame. In the convectively unstable regime, both front velocities and the group velocity of the wave packet have the same direction so that the wave packet is blown out of the system according to the linear dynamics. In the absolutely unstable regime, however, one of the front velocities is directed oppositely to the other and the signs of the front velocities are different (cf. Sec. IV B below). Thus, in the absolutely unstable regime, the initially localized vortex perturbation expands and grows in both axial directions. At the boundary between both regimes, one front is stationary in the laboratory frame.

In order to find this boundary, which is indicated in the following by the index "c-a," we use a saddle-point analysis for $\sigma(Q)$ as well as for $\sigma_{\mathrm{GLE}}(Q)$. The necessary saddle-point conditions of a nongrowing and nontraveling front in the laboratory frame [4,20,23] read

$$\mathrm{Re}\,\sigma(Q)|_{Q_s,\mu_s} = 0, \qquad \left.\frac{d\sigma(Q)}{dQ}\right|_{Q_s,\mu_s} = 0 \tag{4.4}$$

for a saddle of $\sigma(Q)$ that is located at $Q_s = Q_{c\text{-}a}$ with $\mu_s = \mu_{c\text{-}a}$ [23]. The solution of Eq. (4.4) at fixed m, Re, and R_2 yields $\mu_{c\text{-}a}$, i.e., $R_{1,c\text{-}a}$ and $k_{c\text{-}a}, K_{c\text{-}a}, \omega_{c\text{-}a}$.

1. *Saddle points and fronts*

We investigate here the saddle points for $m = 2$. The saddles that are of interest for our stability analysis lie on curves in k-K-R_1 space that intersect the marginal stability surface $R_{1,\mathrm{stab}}(k,K)$. There, perturbations with the spatial variation of exponential fronts of the form $e^{i(Qz+m\varphi)} = e^{i(kz+2\varphi)}e^{Kz}$ have zero temporal growth rate, $\gamma = 0$. We first regard in this section the saddle curves that evolve out of the critical point like the curves labeled I and II in Fig. 7 for the parameter combination $R_2 = 0, \mathrm{Re} = 0$ as a representative example. Thereafter, we briefly discuss other saddle points that may occur elsewhere in k-K-R_1 space, e.g., for $K \neq 0$ like the one labeled III in Fig. 7.

In Fig. 7, the critical point $(k_c, K = 0, R_{1,c})$ is marked by a filled circle. There, a pair of saddles always occurs, and close to the critical point they have different signs in K, i.e., they characterize fronts of type + (saddle I in Fig. 7) and − (saddle II in Fig. 7). The two fronts enclose as envelopes the two sides of wave packets that consist of near-critical extended L2 SPI modes. For more details concerning fronts of the form $e^{i(k_S z-\omega_S t+m\varphi)}e^{K_S(z-w_S t)}$ in the laboratory frame that are represented by a particular saddle S, see Sec. IV B and [20].

For the parameters of Fig. 7, the velocity w_{II} of the − front labeled II is always positive so that this envelope of the wave packet continues to propagate axially upward when R_1 is increased beyond $R_{1,c}$. The + front labeled I, however, changes twice its propagation direction with increasing R_1: between

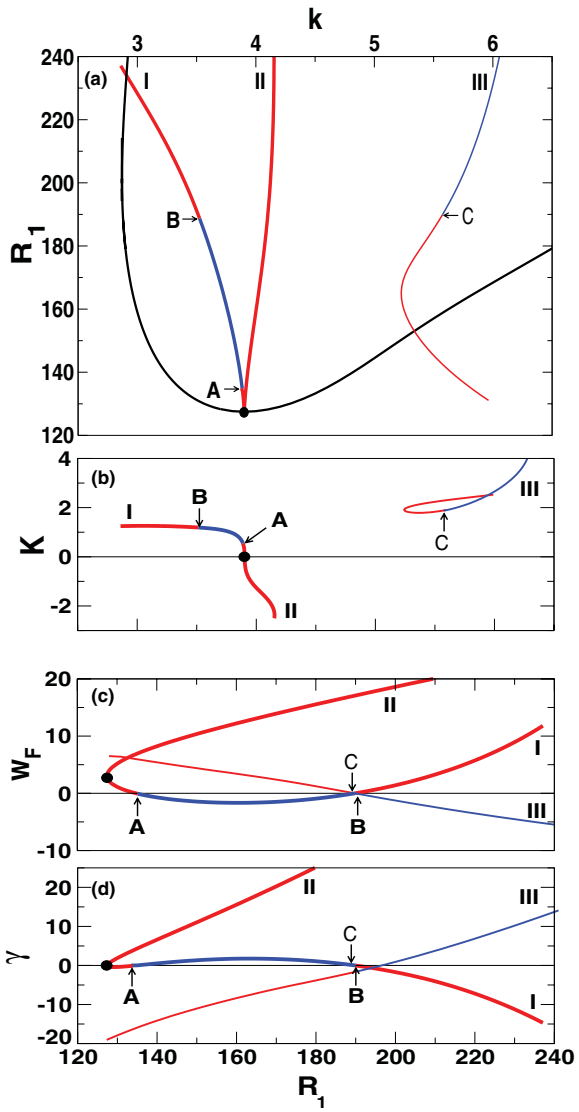

FIG. 7. (Color online) Saddle points and front properties of L2 SPI perturbations for $R_2 = 0$, Re $= 0$. Curves labeled I, II, and III refer to three different saddle points of $\sigma(Q) + iw_F Q$ describing fronts; cf. Sec. IV B. Here, I and III describe + fronts with $K > 0$ while II represents a − front with $K < 0$. The saddle locations projected onto the k-R_1 plane are shown in (a) together with the marginal stability curve for extended $M = 2$ SPI perturbations (full black line). The variation of the spatial growth rates K of the fronts with k is shown in (b). (c) gives the front velocities w_F and (d) the temporal growth rates γ at the respective saddle location as functions of R_1. The critical point $(k_c, R_{1,c}, \gamma = 0, K = 0)$ is marked by a filled circle. At the points labeled A and B, the velocity w_F of the + front I changes sign. Front III reverts its propagation direction at point C.

the critical point (filled circle) and point A ($R_1 = 134.9$) $w_{\rm I}$ is positive, between A and B ($R_1 = 189.4$) it is negative, and then $w_{\rm I}$ is again positive beyond point B as $w_{\rm II}$. Thus, in the interval between $R_{1,c}$ and A, the basic flow is convectively unstable against localized L2 SPI perturbations. Then, at A the system enters into the absolutely unstable regime. But, most interestingly, beyond B the system reenters again the convectively unstable regime since the + and − fronts I and II both move axially upward again. To summarize, points A and B mark stability boundaries between convectively and absolutely unstable regimes against L2 SPI perturbations with wave numbers k that are close to the critical one, k_c.

For sufficiently large negative Re, however, both fronts of a wave packet that develops out of critical L2 SPI perturbations move first, i.e., for near-critical values of R_1 axially downward into the direction of the through flow. Then, one enters with increasing R_1 the absolutely unstable regime when the − front changes its propagation direction and moves upward against the "wind" of the through flow. Finally, for even larger R_1, the + front reverts its propagation direction so that with both fronts now moving axially upward one enters again the convectively unstable domain.

Besides the saddles that originate at the critical point $(k_c, K = 0, R_{1,c})$, there exist for other control parameters further saddles of $\sigma(Q) + iw_F Q$ at other Q. They represent L2 SPI fronts with other front characteristics for perturbations that grow or decay in the laboratory frame under the respective front. For the parameters that we have investigated here, we always found other fronts under which other L2 SPI perturbations other than those described by saddles I and II would grow out of the basic state at large R_1. This holds in particular for the convectively unstable parameter domain at large R_1 defined by the aforementioned fronts I and II. Thus, the reappearance of the convectively unstable behavior at larger R_1 strictly refers only to saddles I and II originating at the critical point. We have chosen here saddle III in Fig. 7 as a representative for all the other ones.

The + front represented by saddle III changes its propagation direction at point C ($R_1 = 187.8$). Below this value of R_1, spatially bounded L2 SPI perturbations characterized by saddle III with the large wave numbers $k > 5$ shown in Fig. 7(b) are blown out of the system under the axially upward moving front III. However, for R_1 values beyond point C, the front III moves axially downward so that under the envelope of this + front, L2 SPI perturbations expand axially downward. Thus, according to the linear dynamics investigated here, large-k L2 SPI structures that are originally spatially bounded by the envelope of the + front III will expand beyond point C to fill the whole system.

Finally, we should like to mention that the changes in the propagation direction of the + fronts I and III at points A and C, respectively, seem to be unrelated. For other values of the control parameters R_2 and Re, the R_1 values of A and C differ more than for the case of Fig. 7. Furthermore, the appearance of saddle III close to $R_{1,c}$ in Fig. 7(a) seems to be unrelated to critical behavior. For other parameters, it starts farther away from $R_{1,c}$.

Test calculations showed also for $M = 3$ spiral fronts a similar multitude of saddles in the plane of complex wave numbers and changes of front propagation directions. However, the parameter dependence was not analyzed systematically.

2. *Boundaries between convective and absolute instability*

Here we investigate the Re and R_2 dependence of the boundaries between convective and absolute instability against localized L2 SPI perturbations. Thus, considering the saddle point pair that starts in the critical point, we explore the Re and R_2 dependence of points A and B in Fig. 7 that mark

there the sought-after boundaries. We do not consider in this subsection other saddle points that describe other fronts under which other L2 SPI perturbations might grow and invade the whole system, such as, e.g., front III in Fig. 7.

In Figs. 8(a)–8(c), we show the Re dependence of the reduced boundaries,

$$\epsilon_{c\text{-}a}(\mathrm{Re}) = \frac{R_{1,c\text{-}a}(\mathrm{Re})}{R_{1,c}(\mathrm{Re}=0)} - 1, \tag{4.5}$$

between convective and absolute instability for L2 SPI perturbations at three different R_2. The bifurcation threshold ϵ_c (2.4) of axially extended L2 SPI solutions is included for comparison as well. Both have been obtained via the dispersion relation of the NSE (2.10) by using a shooting method and, in the case of $\epsilon_{c\text{-}a}$, by using the saddle-point analysis leading to Eq. (4.4). The dotted lines labeled $\epsilon_{c\text{-}a}$(GLE) come from the GLE approximation Eq. (4.3) to the dispersion relation.

The surface with the shape of a horn in Fig. 8(d) encloses the absolutely unstable regime of the basic state against L2 SPI perturbations. The shaded areas in Figs. 8(b) and 8(c) show cross sections of the horn at $R_2 = 0$ and -50, respectively. Within the horn, initially localized L2 SPI wave packets expand axially in both directions. In the convectively unstable region outside of the horn above the lower curved ϵ_c surface, L2 SPI wave packets have a positive growth rate but are blown advectively out of the system.

It is not surprising that for sufficiently large through-flow intensity, axially localized L2 SPI perturbations are blown out of the system. For example, for $R_2 = 0$ in Fig. 8(b), absolute instability occurs only in the through-flow interval $-4.93 < \mathrm{Re} < 2.28$. Outside of it, the basic flow is only convectively unstable against localized L2 SPI perturbations. But it is somewhat unusual that the absolutely unstable parameter domain is closed also at large driving R_1 by a convectively unstable surrounding. Furthermore, the absolutely unstable region pinches off at the tip of the horn in Fig. 8(d), i.e., when R_2 is positive and sufficiently large. Thus, e.g., in Fig. 8(a) absolute instability no longer occurs at $R_2 = 50$ according to the NSE.

The GLE approximation, on the other hand, displays an absolute instability there. In fact, the GLE approximation fails completely to reproduce the horn structure of the absolutely unstable domain in Fig. 8(d) with the associated reentrance of the system into convective instability. The jump of $\epsilon_{c\text{-}a}$(GLE) in Fig. 8(b) at $\mathrm{Re} \approx -6.4$ is tied to the jump of the minimum of the marginal stability curve discussed in Sec. III since the GLE approximation is an expansion around ϵ_c, k_c, which undergo a jump.

As an aside, we mention that the tip of the horn in Fig. 8(d) lies close to the parameters where ϵ_c first undergoes a jump as a consequence of the disappearance of the islands discussed in Fig. 4 with increasing R_2 and with Re becoming more negative.

To sum up, the horn structure of the absolutely unstable domain in Fig. 8(d) implies that localized L2 SPI perturbations expanding out of the extended state are blown out of the system whenever one (or more) of the following three conditions holds: (i) the through-flow intensity |Re| is sufficiently strong, (ii) R_1 is too large, or (iii) R_2 is large enough.

The horn in Fig. 8(d) and similarly the island in Fig. 8(b) are absolutely unstable regions against the growth of localized

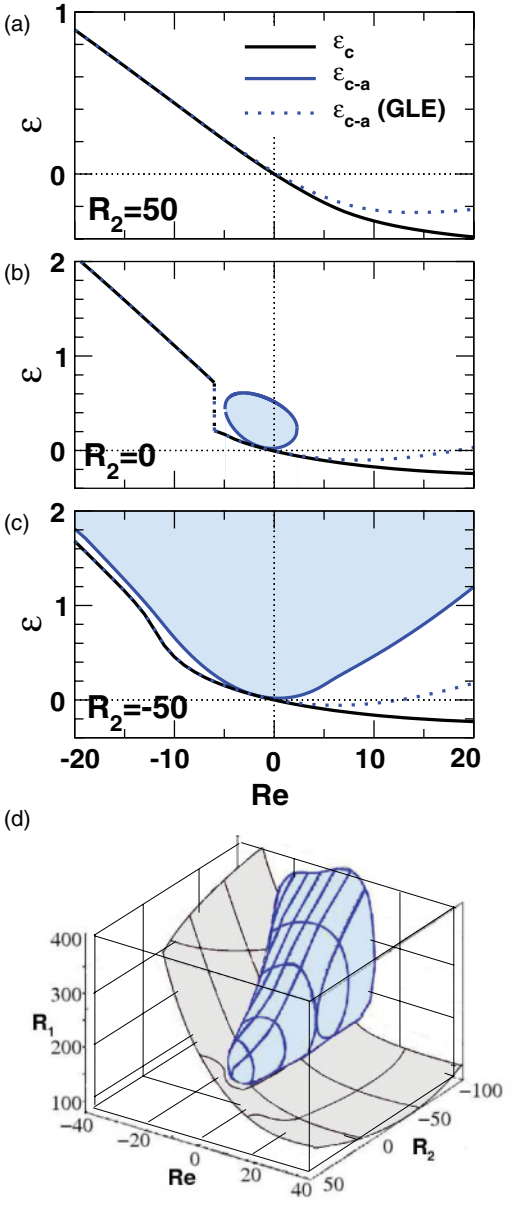

FIG. 8. (Color online) Absolute and convective instability of the basic CCF APF state against L2 SPI perturbations as a function of Re and R_2. The horn-shaped surface in R_1-R_2-Re space shown in (d) is the boundary between the absolutely unstable regime within the horn and the convectively unstable regime. The lines on the horn at nonequidistant values of R_2 and Re are included to better show the shape of the horn. The curved open surface in (d) below the horn is the critical bifurcation threshold ϵ_c for axially extended L2 SPI solutions, i.e., the marginal stability surface of the basic state against L2 SPI with the critical wave number k_c. (a)–(c) show cross sections through (d) at different R_2, however with the reduced driving ϵ instead of R_1 along the vertical axis. Lines labeled $\epsilon_{c\text{-}a}$ and $\epsilon_{c\text{-}a}$(GLE) are the reduced convective-absolute boundaries following from the NSE and the GLE approximation, respectively. These results were obtained from saddle points of the dispersion relation that emanate from criticality against extended L2 SPI perturbations. In addition, we found also L2 SPI fronts corresponding to other k-K saddle locations that destroy the basic flow state at control parameters within the horn and in the convectively unstable domain.

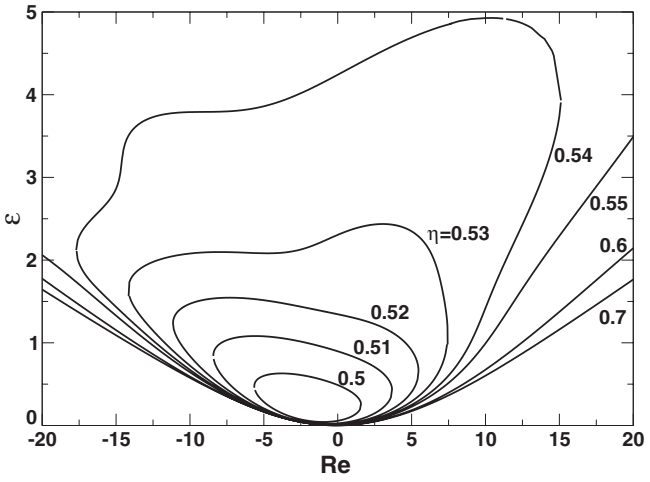

FIG. 9. Thresholds $\epsilon_{c\text{-}a}(\mathrm{Re})$ of the absolutely unstable regime against L2 SPI perturbations vs through-flow Reynolds number Re for different radius ratios η and $R_2 = 0$. As in Fig. 8, these thresholds come from saddles that evolve out of critical extended L2 SPI perturbations when R_1 is increased.

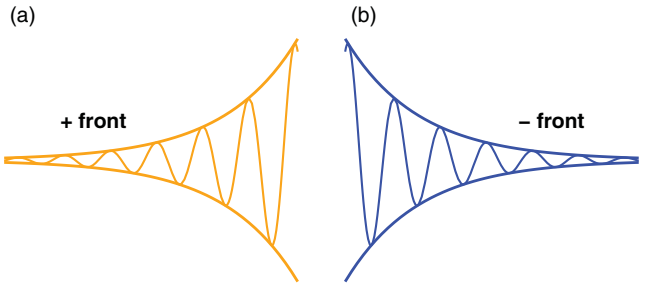

FIG. 10. (Color online) Schematic snapshots of the axial variation of a vortex pattern (thin lines) under the exponentially varying envelopes (thick lines) of an orange (bright gray) + front and of a blue (dark gray) − front. Pattern growth and expansion into the unstructured basic state can occur when the + front moves to the left, i.e., for $w_F^+ < 0$ or when the − front moves to the right, i.e., for front velocities $w_F^- > 0$. Otherwise, the vortex perturbation moves out of the system.

L2 SPI wave packets out of the basic state. These regions are surrounded by a regime of convective instability. That has to be contrasted with the instability islands discussed in Sec. III, which are regions with positive linear growth, $\gamma(k) > 0$, for extended L2 SPI perturbations with axial wave number k. These islands are completely surrounded by a regime in which $\gamma(k) < 0$. So, $\gamma(k) > 0$ islands occur when the $\gamma(k) = 0$ plane lies between the top of the hill and the saddle of the $\gamma(k)$ surface over, say, the k-R_1 plane, cf. Fig. 3. However, in the case of the islands of the absolute-convective stability boundary, a saddle of $\sigma(Q)$ necessarily crosses the $\gamma = 0$ plane in order to fulfill the condition Eq. (4.4).

Finally, we mention that the absolute instability region also varies when changing the system geometry η as shown in Fig. 9. Larger radius ratios η expand the region of absolute instability while smaller ones let them shrink.

B. Fronts

Here we investigate front properties of L2 SPI perturbations described by the linearized NSE and compare them with those following from the GLE approximation. The saddle conditions for fronts that move with velocity w_F in the laboratory frame and that show neither growth nor decay in the frame comoving with the front velocity w_F read

$$\frac{d}{dQ}[\sigma(Q) + iQw_F] = 0 \quad \text{and} \quad \mathrm{Re}[\sigma(Q) + iQw_F] = 0. \tag{4.6}$$

Here we present only results for the saddles that develop out of the ones representing critical L2 SPI perturbations with $Q = k_c$ at $R_{1,c}$. We distinguish between + fronts and − fronts according to whether there is exponential vortex growth or decay, respectively, with increasing z, as shown schematically in Fig. 10.

In Fig. 11, several properties of the blue (dark gray) − front as well as of the orange (bright gray) + front of L2 SPI perturbations are plotted as functions of μ for fixed $R_2 = 0$ and different through-flow Reynolds numbers Re = 1,5,10,15 as indicated. Solid lines refer to the NSE and dashed lines to its GLE approximation. The presented front and saddle properties, respectively, are the spatial growth rate K_S of the front, the wave number k_S of the vortex pattern under the front, the front velocity w_S, and the frequency ω_S of the L2 SPI perturbation under the front. $Q_S = k_S - iK_S$ is the location of the saddle in the complex wave-number plane.

At $\mu = 0$, where the saddles in question develop out of the critical wave number $Q_S = k_c$, the respective properties of − fronts and + fronts fall together with $K_S = 0$. Wave packets limited by two fronts with nonzero K can grow only above the critical threshold at $\mu > 0$.

Comparing the NSE results for L2 SPI fronts with those of the GLE approximation, one sees partly large discrepancies as found already in Fig. 8 for the convective-absolute threshold. The GLE has difficulties in describing the front behavior of L2 SPI structures since all quantities differ dramatically from those of the NSE. Similar differences were also observed for TVF and 1 SPI at larger μ for, e.g., frequencies and wave numbers [20]. Here, all quantities are concerned and the differences occur already for small μ.

Most consequential for the convective-absolute threshold is that the velocities of the + fronts resulting from the GLE always change exactly once their sign, namely at the location indicated by $\mu_{c\text{-}a}^{\mathrm{GLE}}$ in Fig. 11. Thus, the GLE always predicts for the parameters of Fig. 11 an absolute unstable regime for $\mu > \mu_{c\text{-}a}^{\mathrm{GLE}}$. On the other hand, the + fronts of the NSE either change their propagation direction twice, namely at $\mu_{c\text{-}a}^{\mathrm{NSE}}$, or their propagation direction never changes, as in Fig. 11 for the larger values of Re. Thus, the absolutely unstable μ interval predicted by the NSE for L2 SPI perturbations is either limited or not existent for the parameters of Fig. 11. See also Fig. 8(b). There, the absolutely unstable regime for the case $R_2 = 0$ can be seen to shrink with increasing positive Re and to pinch off at Re = 2.28.

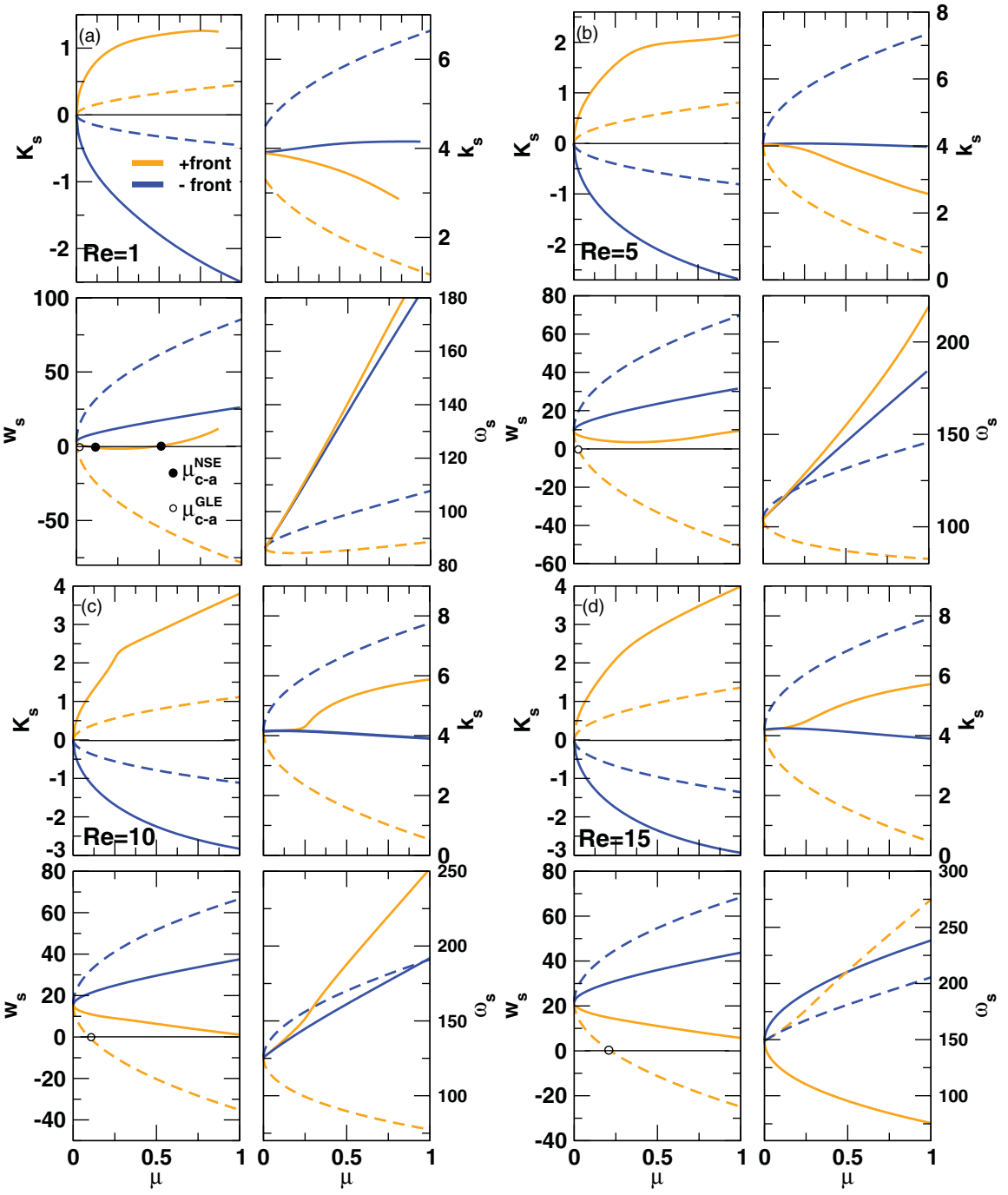

FIG. 11. (Color online) Spatiotemporal characteristics of orange (bright gray) + and blue (dark gray) − fronts of near-critical localized L2 SPI wave packets for $R_2 = 0$ and different through-flow Reynolds numbers Re = 1,5,10,15 (a)–(d) as indicated. In each case, the axial growth rate K_s, the wave number k_S, the front velocity w_S, and the frequency ω_S are shown for both fronts vs μ. Solid lines refer to the NSE and dashed lines to its GLE approximation. The locations of the boundaries between convective and absolute instability are indicated by μ_{c-a}^{NSE} (filled circle) and by μ_{c-a}^{GLE} (open circle).

V. CONCLUSION

We have determined the influence of an axial through flow on the spatiotemporal growth behavior of axially extended as well as of localized vortex structures in the Taylor-Couette system by solving the linearized Navier-Stokes equations numerically for perturbations with an azimuthal wave number $M = 2$ in a wide range of the parameters Re, R_1, R_2, and η. While the presentation of our results is focused largely on L SPI structures, the corresponding results for R SPI structures are included as well: because of the $z \to -z$ symmetry of the Taylor-Couette system, an R SPI at a Reynolds number Re behaves like the mirror image of an L SPI at −Re.

In the first part, we have calculated the marginal and critical bifurcation thresholds of axially extended vortex structures out of the unstructured basic flow state of CCF APF. For these,

we found a new, unexpected, and so far unknown behavior: for certain control parameter combinations, the marginal stability boundary of the basic flow is not represented by a single curve in the k-R_1 plane as for structures with azimuthal wave numbers $M \leqslant 1$. Rather, the bifurcation threshold of, say, extended L2 SPI vortex structures splits up into separate curves when the through-flow Reynolds number Re is sufficiently negative. The same occurs for the R2 SPI bifurcation threshold when Re is positive and sufficiently large. Thereby, an island is formed in the k-R_1 plane in which, e.g., L2 SPI solutions can grow and saturate nonlinearly. Outside of this island, extended L2 SPI perturbations become extinct. We found this to be the result of an eigenvalue surface $\gamma(R_1,k)$ that is much more complicated than that of $M \leqslant 1$ perturbations. Another consequence of this complexity are discontinuities in the critical values, say, as a function of Re and R_2. We also found that changing the through flow and changing the outer cylinder's rotation rate has similar effects on the bifurcation thresholds of extended L2 SPI vortex structures.

In the second part, we have determined the boundaries $R_{1,c\text{-}a}(R_2,\mathrm{Re},\eta)$ between convective and absolute instability against localized L2 SPI perturbations using a saddle-point analysis. To that end, we determined the complex dispersion relation $\sigma(Q)$ of the linearized NSE over the plane of complex wave numbers $Q = k - iK$ and in addition that of the Ginzburg-Landau approximation.

We have investigated the saddle-point pair in the Q plane that evolves with increasing R_1 out of the one for extended critical L2 SPI perturbations with $k = k_c$ and $K = 0$ at $R_{1,c}$. This pair describes for slightly supercritical R_1 the two fronts of a wave packet of L2 SPI perturbations. For them we found within the NSE, but not within the GLE, an unusual behavior, namely finite R_1 intervals of absolute instability bounded not only from below but also from above by a convectively unstable regime. In other words, the basic flow becomes with increasing R_1 first convectively unstable to localized L2 SPI perturbations, then absolutely unstable, and then again convectively unstable. In R_1-R_2-Re parameter space, the absolutely unstable regime has the shape of a horn. It implies in turn that outside of the horn, localized L2 SPI perturbations growing in the basic flow are blown out of the system, that is, whenever one (or more) of the following three conditions holds: (i) the through-flow intensity |Re| is sufficiently strong, (ii) R_1 is too large, or (iii) R_2 is large enough. The GLE approximation does not reproduce this complex behavior. Furthermore, unlike the NSE, it does not show other saddles and fronts with other spatiotemporal properties that could destroy the basic state by an invasion of other L2 SPI structures under such fronts.

In the last part, we presented overviews over the characteristic front properties: spatial growth rate, wave number, front velocity, and frequency of the aforementioned two L2 SPI fronts that evolve with increasing R_1 out of critical extended perturbations and how they change with through flow. Also here the GLE does not provide good results.

To summarize, we found two types of "growth islands" for L2 SPI vortices and thus similarly also for R2 SPI vortices. The first type of island appears in a through flow of sufficient strength that is directed downward for L2 SPI and upward for R2 SPI, i.e., opposite to the direction into which the respective vortices propagate for $\mathrm{Re} = 0$. The island is a region in the k-R_1 plane with $\gamma > 0$ where axially extended 2 SPI perturbations can grow. Such a region is bounded by the bifurcation threshold, $\gamma = 0$, for extended 2 SPI solutions in the form of a closed curve, and it is surrounded by a $\gamma < 0$ regime. The second type of island is a region in the Re-R_1 parameter plane where the basic flow is absolutely unstable against localized 2 SPI perturbations bounded by two fronts that evolve with increasing R_1 out of the critical point. This region is surrounded by a convectively unstable regime.

ACKNOWLEDGMENTS

We thank the Deutsche Forschungsgemeinschaft for support.

[1] R. C. DiPrima and H. L. Swinney, in *Hydrodynamic Instabilities and the Transition to Turbulence*, No. 45 in *Topics in Applied Physics*, edited by H. L. Swinney and J. G. Gollub (Springer, Berlin, 1985).
[2] R. J. Donnelly, Phys. Today **44**(11), 32 (1991).
[3] R. Tagg, Nonlinear Sci. Today **4**, 1 (1994).
[4] M. C. Cross and P. C. Hohenberg, Rev. Mod. Phys. **65**, 851 (1993).
[5] P. Chossat and G. Iooss, *The Couette-Taylor Problem* (Springer, Berlin, 1994).
[6] Ch. Hoffmann and M. Lücke, in *Physics of Rotating Fluids* (Springer-Verlag, Berlin, 2000), pp. 55–66.
[7] M. Golubitsky and I. Stewart, SIAM J. Math. Anal. **17**, 249 (1986).
[8] M. Golubitsky, I. Stewart, and D. Schaeffer, in *Singularities and Groups in Bifurcation Theory II* (Springer, New York, 1988), pp. 485–512.
[9] W. F. Langford, R. Tagg, E. J. Koestlich, H. L. Swinney, and M. Golubitzky, Phys. Fluids **31**, 776 (1988).
[10] R. C. DiPrima and A. Pridor, Proc. R. Soc. London, Ser. A **366**, 555 (1979).
[11] D. I. Takeuchi and D. F. Jankowski, J. Fluid Mech. **102**, 101 (1981).
[12] B. S. Ng and E. R. Turner, Proc. R. Soc. London, Ser. A **382**, 83 (1982).
[13] Th. Gebhardt and S. Grossmann, Z. Phys. **90**, 475 (1993).
[14] A. Meseguer and F. Marques, J. Fluid Mech. **455**, 129 (2002).
[15] R. Tagg, W. S. Edwards, and H. L. Swinney, Phys. Rev. A **42**, 831 (1990).
[16] K. L. Babcock, D. S. Cannell, and G. Ahlers, Physica D **61**, 40 (1992).
[17] K. L. Babcock, G. Ahlers, and D. S. Cannell, Phys. Rev. E **50**, 3670 (1994).

[18] R. Tagg, W. S. Edwards, and H. L. Swinney, Phys. Rev. A **42**, 831 (1990).
[19] A. Recktenwald, M. Lücke, and H. W. Müller, Phys. Rev. E **48**, 4444 (1993).
[20] A. Pinter, M. Lücke, and Ch. Hoffmann, Phys. Rev. E **67**, 026318 (2003).
[21] I. Mutabazi and A. Bahloul, Theor. Comput. Fluid Dyn. **16**, 79 (2002).
[22] Ch. Hoffmann, M. Lücke, and A. Pinter, Phys. Rev. E **69**, 056309 (2004).
[23] P. Huerre and P. A. Monkewitz, Annu. Rev. Fluid Mech. **22**, 473 (1990).